

Large anomalous Nernst and spin Nernst effects in noncollinear antiferromagnets Mn_3X ($X = \text{Sn, Ge, Ga}$)

Guang-Yu Guo^{1, 2, *} and Tzu-Cheng Wang³

¹*Department of Physics and Center for Theoretical Physics,
National Taiwan University, Taipei 10617, Taiwan*

²*Physics Division, National Center for Theoretical Sciences, Hsinchu 30013, Taiwan*

³*Department of Physics and Center for Theoretical Sciences,
National Taiwan University, Taipei 10617, Taiwan*

(Dated: April 8, 2021)

Noncollinear antiferromagnets have recently been attracting considerable interest partly due to recent surprising discoveries of the anomalous Hall effect (AHE) in them and partly because they have promising applications in antiferromagnetic spintronics. Here we study the anomalous Nernst effect (ANE), a phenomenon having the same origin as the AHE, and also the spin Nernst effect (SNE) as well as AHE and the spin Hall effect (SHE) in noncollinear antiferromagnetic Mn_3X ($X = \text{Sn, Ge, Ga}$) within the Berry phase formalism based on *ab initio* relativistic band structure calculations. For comparison, we also calculate the anomalous Nernst conductivity (ANC) and anomalous Hall conductivity (AHC) of ferromagnetic iron as well as the spin Nernst conductivity (SNC) of platinum metal. Remarkably, the calculated ANC at room temperature (300 K) for all three alloys is huge, being 10~40 times larger than that of iron. Moreover, the calculated SNC for Mn_3Sn and Mn_3Ga is also larger, being about five times larger than that of platinum. This suggests that these antiferromagnets would be useful materials for thermoelectric devices and spin caloritronic devices. The calculated ANC of Mn_3Sn and iron are in reasonably good agreement with the very recent experiments. The calculated SNC of platinum also agrees with the very recent experiments in both sign and magnitude. The calculated thermoelectric and thermomagnetic properties are analyzed in terms of the band structures as well as the energy-dependent AHC, ANC, SNC and spin Hall conductivity via the Mott relations.

PACS numbers:

I. INTRODUCTION

In recent two decades, spin transport electronics (spintronics) has attracted enormous interest because of its promising applications in information storage and processing and other electronic technologies^{1, 2}. Spin current generation, detection and manipulation are three key issues in the spintronics. In this context, spin-related transport phenomena in solids especially in those materials that can provide highly spin-polarized charge current and large pure spin current, have been intensively investigated recently. The anomalous Hall effect (AHE), discovered in 1881 by Hall³, and the spin Hall effect (SHE), predicted in 1971 by Dyakonov and Perel⁴, are two principal spin-related transports and thus have received renewed interests.^{5, 6} Intuitively, spin-up and spin-down electrons moving through the relativistic band structure of a solid experience opposite transverse velocities caused by an applied electric field. In a ferromagnet where an unbalance of spin-up and spin-down electrons exists, these opposite currents result in a spin-polarized transverse charge current and hence the (intrinsic) AHE. Therefore, the AHE is usually assumed to be proportional to the magnetization of the magnetic material. In a nonmagnetic material where spin-up and spin-down electrons are equal in numbers, this process gives rise to a pure transverse spin current, and this is known as the (intrinsic) SHE. The SHE is particularly important for spintronics be-

cause it enables us to generate, detect and control spin current without magnetic field or magnetic materials.^{6, 7} Furthermore, the pure spin current is dissipationless⁸ and is thus especially useful for the development of low power-consumption nanoscale spintronic devices⁹.

Interestingly, Chen *et al.*¹⁰ recently showed that large AHE could occur in noncollinear antiferromagnets without net magnetization such as cubic Mn_3Ir . This surprising result arises from the fact that in a three-sublattice kagome lattice with a noncollinear triangle antiferromagnetic structure, not only the time-reversal symmetry (\mathcal{T}) is broken but also there is no spatial symmetry operation (\mathcal{S}) which, in conjunction with \mathcal{T} , is a good symmetry that preserves the Kramers theorem. Subsequently, large AHE was observed in hexagonal noncollinear antiferromagnets Mn_3Sn ¹¹ and Mn_3Ge ^{12, 13}. In the meantime, large SHE was predicted in noncollinear antiferromagnets Mn_3X ($X = \text{Sn, Ge, Ir}$)^{14, 15} and was also observed in Mn_3Ir ¹⁵. All these fascinating findings suggest that these noncollinear antiferromagnets may find exciting applications in spintronics, an emergent field called antiferromagnetic spintronics¹⁶. Antiferromagnetic spintronics has been attracting increasing attention in recent years because antiferromagnetic materials have several advantages over ferromagnetic materials. In particular, antiferromagnetic elements would not magnetically affect their neighbors and are insensitive to stray magnetic fields. Moreover, antiferromagnets have faster spin dynamics than ferromagnets, and this would lead to ultra-

fast data processing.

In a ferromagnet, the charge Hall current could also arise when a temperature gradient (∇T) instead of an electric field, is applied. This phenomenon, due to the simultaneous presence of the spin-orbit coupling (SOC) and net magnetization in the ferromagnet, is referred to as the anomalous Nernst effect (ANE)¹⁷⁻¹⁹. Similarly, a temperature gradient could also generate the spin Hall current in a nonmagnetic material, and this is known as the spin Nernst effect (SNE)²⁰. Clearly, materials that exhibit large ANE and SNE would have useful applications for spin thermoelectronic devices driven by heat, a new field known as spin caloritronics²¹. This offers exciting prospects of 'green' spintronics powered by, e.g., waste ohmic heat. Since the ANE and SNE, respectively, have the same physical origins as the AHE and SHE, one could expect significant ANE and SNE in the above-mentioned noncollinear antiferromagnets as well. In other words, noncollinear antiferromagnets Mn_3X ($X = Sn, Ge, Ga$) could also be useful materials for developing antiferromagnetic spin caloritronics. Nevertheless, no investigation of the SNE in noncollinear antiferromagnets has been reported and only two reports on the measurement of the ANE in Mn_3Sn appeared very recently.^{22,23}

In this paper, therefore, we perform an *ab initio* study on the ANE and SNE in hexagonal noncollinear antiferromagnets Mn_3Ga , Mn_3Ge and Mn_3Sn (Fig. 1), based on the density functional theory (DFT) with the generalized gradient approximation (GGA)²⁴. For comparison, we also study the ANE in bcc Fe, a ferromagnetic transition metal having large AHE²⁵, and the SNE in fcc Pt, a heavy nonmagnetic transition metal exhibiting gigantic SHE²⁶. Indeed, we find that the anomalous Nernst conductivity at room temperature of all three alloys is large, being more than ten times larger than that of bcc Fe. The spin Nernst conductivity of Mn_3Ga and Mn_3Sn is larger than that of fcc Pt. The rest of this paper is organized as follows. In the next section, we briefly describe the Berry phase formalism for calculating the intrinsic Hall and Nernst conductivities as well as the computational details. Section III consists of three subsections. We first present the calculated total energy and magnetic properties of two low-energy noncollinear antiferromagnetic structures [Figs. 1(c) and 1(d)] of Mn_3X and also compared our results with available previous experimental and theoretical reports in Subsec. III A. We then report the calculated anomalous Nernst conductivity as well as anomalous Hall conductivity for these magnetic structures in Subsec. III B. We finally present the calculated spin Nernst conductivity and also spin Hall conductivity in Subsec. III C. Finally, the conclusions drawn from this work are summarized in Sec. IV.

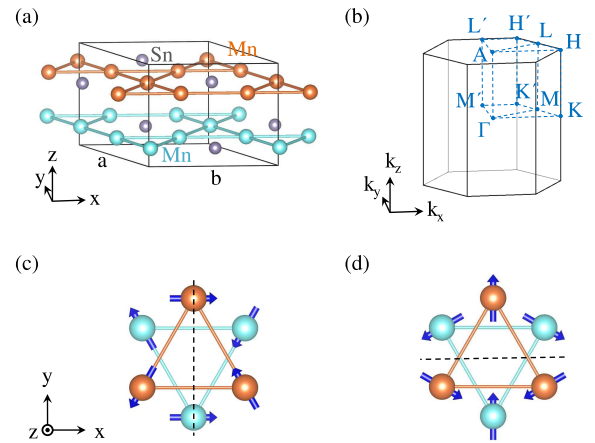


FIG. 1: (Color online) (a) Layered hexagonal (D_{6h}^4) structure of Mn_3X ($X = Sn, Ge, Ga$) with (b) the associated hexagonal Brillouin zone (BZ). (c) Type A and (d) type B antiferromagnetic configurations considered in this paper. Both magnetic structures have an orthorhombic symmetry and thus their irreducible BZ wedge (IBZW) [i.e., the trapzian prism indicated by the blue dashed lines in (b)] is three times larger than the hexagonal IBZW [i.e., the triangle prism indicated by the blue dashed lines in (b)]. The vertical [horizontal] black dashed line in (c) [(d)] denotes the mirror plane.

II. THEORY AND COMPUTATIONAL METHOD

Here we consider ordered Mn_3Ga , Mn_3Ge and Mn_3Sn alloys in the layered hexagonal DO_{19} ($P6_3/mmc$ or D_{6h}^4) structure [see Fig. 1(a)] and use the experimental lattice constants of $a = 5.36 \text{ \AA}$ and $c = 4.33 \text{ \AA}$ ²⁷, $a = 5.34 \text{ \AA}$ and $c = 4.31 \text{ \AA}$ ¹², and $a = 5.66 \text{ \AA}$ and $c = 4.53 \text{ \AA}$ ¹¹, respectively. The primitive unit cell contains two layers of Mn triangles stacked along the c -axis, and in each layer the three Mn atoms form a kagome lattice with the X atom located at the center of each hexagon (Fig. 1). The total energy and electronic structure are calculated based on the DFT with the GGA in the form of Perdew-Burke-Ernzerhof²⁴. The accurate projector-augmented wave (PAW) method²⁸, as implemented in the Vienna *ab initio* simulation package (VASP)^{29,30}, is used. The fully relativistic PAW potentials are adopted in order to include the SOC. The valence configurations of Mn, Sn, Ge and Ga atoms taken into account in the calculations are $3d^64s^1$, $4d^{10}5s^25p^2$, $3d^{10}4s^24p^2$ and $3d^{10}4s^24p^1$, respectively. A large plane-wave cutoff energy of 350 eV is used throughout. In the self-consistent electronic structure calculations, a fine Γ -centered \mathbf{k} -point mesh of $20 \times 20 \times 20$ [i.e., 2112 \mathbf{k} -points over the orthorhombic irreducible Brillouin zone wedge (IBZW) (see Fig. 1)] is adopted for the Brillouin zone (BZ) integration using the tetrahedron method³¹.

The anomalous Hall conductivity (AHC) and anomalous Nernst conductivity (ANC) are calculated based on

the elegant Berry-phase formalism³². Within this Berry-phase formalism, the AHC ($\sigma_{ij}^A = J_i^c/E_j$) is simply given as a BZ integration of the Berry curvature for all the occupied bands,

$$\sigma_{ij}^A = -\frac{e^2}{\hbar} \sum_n \int_{BZ} \frac{d\mathbf{k}}{(2\pi)^3} f_{\mathbf{k}n} \Omega_{ij}^n(\mathbf{k}),$$

$$\Omega_{ij}^n(\mathbf{k}) = - \sum_{n' \neq n} \frac{2\text{Im}[\langle \mathbf{k}n | v_i | \mathbf{k}n' \rangle \langle \mathbf{k}n' | v_j | \mathbf{k}n \rangle]}{(\epsilon_{\mathbf{k}n} - \epsilon_{\mathbf{k}n'})^2}, \quad (1)$$

where $f_{\mathbf{k}n}$ and $\Omega_{ij}^n(\mathbf{k})$ are the Fermi distribution function and the Berry curvature for the n th band at \mathbf{k} , respectively. i and $j \in (x, y, z)$, and $i \neq j$. J_i^c is the i -component of the charge current density \mathbf{J}^c and E_j is the j -component of the electric field \mathbf{E} . Moreover, the ANC ($\alpha_{ij}^A = -J_i^c/\nabla_j T$) can be written as

$$\alpha_{ij}^A = \frac{1}{T} \frac{e}{\hbar} \sum_n \int_{BZ} \frac{d\mathbf{k}}{(2\pi)^3} \Omega_{ij}^n(\mathbf{k})$$

$$\times [(\epsilon_{\mathbf{k}n} - \mu) f_{\mathbf{k}n} + k_B T \ln(1 + e^{-\beta(\epsilon_{\mathbf{k}n} - \mu)})], \quad (2)$$

where μ is the chemical potential and k_B is the Boltzmann constant.^{19,33}

The Berry curvature $\Omega_{ij}^n(\mathbf{k})$ can be considered as a pseudovector³², just like the spin, and thus can be written as $[\Omega_n^x(\mathbf{k}), \Omega_n^y(\mathbf{k}), \Omega_n^z(\mathbf{k})] = [\Omega_{yz}^n(\mathbf{k}), \Omega_{zx}^n(\mathbf{k}), \Omega_{xy}^n(\mathbf{k})]$. Thus, $\Omega_n(\mathbf{k}) = \Omega_n(-\mathbf{k})$ if the system has spatial inversion symmetry (\mathcal{P}) and $\Omega_n(\mathbf{k}) = -\Omega_n(-\mathbf{k})$ if it has \mathcal{T} symmetry.³² Obviously, if the system has both \mathcal{P} and \mathcal{T} symmetries, $\Omega_n(\mathbf{k})$ becomes identically zero. The AHC and ANC are also pseudovectors and can be written as $[\sigma_A^x, \sigma_A^y, \sigma_A^z] = [\sigma_{yz}^A, \sigma_{zx}^A, \sigma_{xy}^A]$ and $[\alpha_A^x, \alpha_A^y, \alpha_A^z] = [\alpha_{yz}^A, \alpha_{zx}^A, \alpha_{xy}^A]$, respectively.

Similarly, the spin Hall conductivity ($\sigma_{ij}^s = J_i^s/E_j$) is given by a BZ integration of the spin Berry curvature ($\Omega_{ij}^{n,s}(\mathbf{k})$) for all the occupied bands,

$$\sigma_{ij}^s = -e \sum_n \int_{BZ} \frac{d\mathbf{k}}{(2\pi)^3} f_{\mathbf{k}n} \Omega_{ij}^{n,s}(\mathbf{k}),$$

$$\Omega_{ij}^{n,s}(\mathbf{k}) = - \sum_{n' \neq n} \frac{2\text{Im}[\langle \mathbf{k}n | \{\tau_s, v_i\} / 4 | \mathbf{k}n' \rangle \langle \mathbf{k}n' | v_j | \mathbf{k}n \rangle]}{(\epsilon_{\mathbf{k}n} - \epsilon_{\mathbf{k}n'})^2}, \quad (3)$$

where s denotes the spin direction and τ_s is a Pauli matrix.²⁶ Then the spin Nernst conductivity ($\alpha_{ij}^s = -J_i^s/\nabla_j T$) can be written as

$$\alpha_{ij}^s = \frac{1}{T} \sum_n \int_{BZ} \frac{d\mathbf{k}}{(2\pi)^3} \Omega_{ij}^s(\mathbf{k}n)$$

$$\times [(\epsilon_{\mathbf{k}n} - \mu) f_{\mathbf{k}n} + k_B T \ln(1 + e^{-\beta(\epsilon_{\mathbf{k}n} - \mu)})], \quad (4)$$

where J_i^s denotes the i -component of the spin current density \mathbf{j}^s with spin being along the s -axis.

In the AHC, SHC, ANC and SNC calculations, the velocity ($\langle \mathbf{k}n | v_i | \mathbf{k}n' \rangle$) and spin-velocity ($\langle \mathbf{k}n | \{\tau_s, v_i\} / 4 | \mathbf{k}n' \rangle$) matrix elements are obtained from

the self-consistent electronic structure within the PAW formalism.³⁴ To obtain accurate AHC, SHC, ANC and SNC, a dense k -point mesh would be needed.^{25,35} Therefore, we use a very fine mesh of 97344 k -points on the magnetic IBZW (1/8 BZ), together with the tetrahedron method³¹. This is equivalent to a large number of k -points of ~ 778752 in the full BZ, and corresponds to the division of the Γ K line into $n_d = 50$ intervals. Further calculations using $n_d = 20, 30$ and 40 (i.e., 7260, 22272, 51597 k -points in the IBZW, respectively) indicate that the AHC, SHC, ANC and SNC obtained using $n_d = 50$ converge to within a few %. Indeed, the curves of AHC, SHC, ANC and SNC as a function of energy (see Figs. 3-5 below) and also the curves of ANC and SNC as a function of temperature (see Fig. 6 below) obtained with $n_d = 40$ and 50 are indistinguishable. Moreover, the calculated AHC, SHC, ANC and SNC versus the inverse of the number (N_k) of k -points in the IBZW are plotted and fitted to a straight line to get the converged theoretical values listed in Table II below (i.e., the extrapolated values at $N_k = \infty$) (see Refs. [36,37]). Note that the differences between the converged theoretical AHC, SHC, ANC and SNC values and the corresponding $n_d = 50$ values are within a few %. As mentioned before, we also calculate the AHC and ANC of ferromagnetic bcc Fe and the SNC of nonmagnetic fcc Pt for comparison. In the calculation of the AHC and ANC of bcc Fe, we also adopt a very fine mesh of 360396 k -points on the magnetic IBZW (1/16 BZ). In the SHC and SNC calculations for fcc Pt, a very fine grid of 253044 k -points on the magnetic IBZW (1/16 BZ) is used.

III. RESULTS AND DISCUSSION

The energetics of many possible magnetic configurations for Mn₃Sn in the hexagonal DO₁₉ structure has already been investigated with the *ab initio* density functional calculations³⁸⁻⁴⁰. Therefore, in this paper we consider only two low-energy noncollinear triangular antiferromagnetic configurations for Mn₃X (X = Sn, Ge, Ga) [see Fig. 1(c) and Fig. 1(d) in Ref.³⁹], namely, type A and type B configurations as illustrated in Fig. 1(c) and Fig. 1(d), respectively. For comparison, the ferromagnetic state (FM) of Mn₃Ga with magnetic moments in the \hat{x} -direction is also investigated.

A. Magnetic properties

The calculated total energies and spin magnetic moments are listed in Table I, together with the reported experimental values. Table I shows that in all three alloys, magnetic structure A has a lower energy than magnetic structure B, although the total energy difference is in the order of ~ 0.01 meV. This agrees with the magnetic structure observed in earlier neutron diffraction experiments on Mn₃Sn⁴³, Mn₃Ge^{43,44} and Mn₃Ga.²⁷ In

TABLE I: Calculated total energy (E_t) and total spin magnetic moment (m_t^s) as well as averaged Mn spin magnetic moment (m_{Mn}^s) for the A and B magnetic structures of Mn_3X ($X = Sn, Ge, Ga$). Total magnetic moments are parallel to the \hat{x} -axis in configuration A but to the \hat{y} -axis in configuration B. The X atoms have a nearly zero magnetic moment (being less than $0.01 \mu_B$) and thus are not listed. Note that there are two formula units [i.e., $2(Mn_3X)$] per unit cell. For comparison, the results of the magnetic moment direction-constrained calculation for Mn_3Ga in configuration A (denoted A*) and the ferromagnetic calculation for Mn_3Ga with the magnetic moments in the \hat{x} -direction (denoted FM) are given as well. Some previously reported total and Mn spin moments are also listed for comparison.

| | | E_t (meV/cell) | m_{Mn}^s (μ_B /atom) | m_t^s ($10^{-3} \mu_B$ /cell) |
|----------|----|---------------------|--------------------------------|-------------------------------------|
| Mn_3Sn | A | 0.0 | 3.13, 3.0 ^a | 0.1, 12 ^b |
| | B | 0.03 | 3.13 | 22 |
| Mn_3Ge | A | 0.0 | 2.70, 2.4 ^c | 0.9, 42 ^d |
| | B | 0.03 | 2.68 | 2.3, 30 ^e |
| Mn_3Ga | A | 0.0 | 2.75, 2.4 ^f | 11.3 |
| | A* | 0.00 | 2.75 | 0.6 |
| | B | 0.01 | 2.73 | 10.9 |
| | FM | 855 | 2.18 | 13019 |

^aRef. 41 (experiment), ^bRef. 11 (experiment), ^cRef. 42 (experiment), ^dRef. 12 (experiment), ^eRef. 13 (experiment), ^fRef. 27 (experiment).

an earlier DFT calculation for Mn_3Sn ³⁹, configuration A was also found to be slightly lower in total energy than configuration B. Nevertheless, the total energy difference is very small and such a small energy difference is perhaps within the numerical uncertainty. This small energy difference between the two configurations is consistent with the experimental fact that the magnetic moments can be easily rotated in the hexagonal plane by a small magnetic field^{11–13,43,44}. In contrast, the total energy of the FM structure of Mn_3Ga is well above that of the two noncollinear antiferromagnetic structures (Table I).

The calculated Mn spin magnetic moments in all three Mn_3X ($X = Sn, Ge, Ga$) alloys are large, being $\sim 3.0 \mu_B$, while the calculated spin magnetic moments of the X atoms are nearly zero, being less than $\sim 0.01 \mu_B$. Table I indicates that the calculated Mn spin magnetic moments agree fairly well with previous experiments.^{11,27,41} Due to rather strong exchange coupling between large spin magnetic moments on the Mn moments, the Néel temperatures in these Mn-based alloys are as high as 420 K in Mn_3Sn ⁴³, 365 K in Mn_3Ge ⁴⁴ and 470 K in Mn_3Ga ²⁷.

Interestingly, in Mn_3Y ($Y = Ir, Rh, Pt$), the calculated total spin magnetic moment is zero and the two coplanar noncollinear T1 and T2 antiferromagnetic structures have the same total energy in the absence of the SOC.^{10,45} This suggests that the small total magnetic moment obtained with the SOC included in Mn_3Y ($Y = Ir, Rh, Pt$), is induced by the spin-canting caused by the Dzyaloshinskii-Moriya interaction (DMI) (i.e., the SOC). In contrast, the nonzero total spin magnetic moment al-

ready exists in Mn_3X ($X = Sn, Ge, Ga$) even without the SOC. For example, the total spin magnetic moment calculated without the SOC, is $4 \times 10^{-3} \mu_B$ /cell along the \hat{x} -axis in magnetic structure A of Mn_3Sn , being larger than that in the presence of the SOC (Table I). This is because both magnetic structures A and B are orthorhombic with only one mirror plane (Fig. 1). In the A magnetic structure, the mirror plane \mathcal{M}_x is parallel to the yz plane [see Fig. 1(c)]. Since the total magnetic moment \mathbf{m}_t is a pseudovector, $m_{t,y}$ and $m_{t,z}$ that are parallel to the yz plane transform, respectively, to $-m_{t,y}$ and $-m_{t,z}$ under the \mathcal{M}_x reflection, while $m_{t,x}$ remains unchanged. Consequently, $m_{t,y}$ and $m_{t,z}$ must be zero and only $m_{t,x}$ can be nonzero. In the B structure, the mirror plane \mathcal{M}_y is parallel to the zx plane [see Fig. 1(d)], and a mirror reflection plus a translation $\tau = (0, 0, c/2)$ would bring the magnetic structure back onto itself. In this case, only $m_{t,y}$ can be nonzero. The calculated magnetic moments are consistent with these symmetry requirements (Table I). In contrast, the T1 and T2 magnetic structures of Mn_3Y are hexagonal and have three mirror planes,^{10,45} and thus all three components of the magnetic moments must be zero. Furthermore, the calculated total energies of the T1 and T2 structures are the same.

B. Anomalous Nernst effect

Table II lists the calculated anomalous Nernst conductivity (α_{ij}^A), anomalous Hall conductivity (σ_{ij}^A) and density of states at the Fermi level [$N(E_F)$] of Mn_3X ($X = Sn, Ge, Ga$) alloys. As discussed before, the AHC and ANC are pseudovectors, just like the total magnetic moment. Thus, in the A (B) magnetic structure, only α_{yz}^A (α_{zx}^A) and σ_{yz}^A (σ_{zx}^A) can be nonzero. This can also be seen from the \mathbf{k} -space distribution of the Berry curvature $\Omega(\mathbf{k}) = [\Omega^x(\mathbf{k}), \Omega^y(\mathbf{k}), \Omega^z(\mathbf{k})]$, as displayed in Fig. 2 for configuration A of Mn_3Sn . Figure 2(a) shows that in the $k_x k_y$ (i.e., $k_z = 0$) plane, $\Omega^y(\mathbf{k})$ is an odd function of k_x while $\Omega^x(\mathbf{k})$ is an even function of k_x . In Fig. 2(b), $\Omega^z(\mathbf{k})$ is found to be an odd function of k_x while $\Omega^x(\mathbf{k})$ is again an even function of k_x in the $k_x k_z$ (i.e., $k_y = 0$) plane. Consequently, Eqs. (1) and (2) would indicate that σ_{zx}^A and σ_{xy}^A as well as α_{zx}^A and α_{xy}^A should be zero. The present results (Table II) are consistent with these symmetry properties. It is also clear from Table II that the AHC, ANC and $N(E_F)$ for both A and B configurations are very similar. This is consistent with the fact that the two configurations have nearly degenerate total energies and very similar magnetic properties (Table I).

The calculated α_{xy}^A and σ_{xy}^A of iron metal are also listed there for comparison. Table II shows that the AHC of all the Mn_3X alloys is rather large, being in the same order of magnitude as that of ferromagnetic iron with a large net magnetic moment of $2.27 \mu_B$ /atom. Remarkably, all the Mn_3X alloys have a huge ANC, which is $10 \sim 40$ times larger than that of Fe (Table II). This strongly suggests that these noncollinear antiferromag-

TABLE II: Calculated density of states at the Fermi level [$N(E_F)$] (states/eV/spin/f.u.), anomalous Hall conductivity (AHC; σ_H^A) (σ_{yz}^A , σ_{zx}^A) and anomalous Nernst conductivity (ANC; α_N^A) (α_{yz}^A , α_{zx}^A) as well as spin Hall conductivity (SHC) (σ_{xy}^z) and spin Nernst conductivity (SNC) (α_{xy}^z) of Mn_3X ($X = Sn, Ge, Ga$). For comparison, the calculated related properties of bcc Fe (σ_{xy}^A , α_{xy}^A) and fcc Pt (σ_{xy}^z , α_{xy}^z) are also listed. Note that ANC and SNC listed here were calculated at temperature $T = 300$ K. The ANC for Mn_3Sn in brackets were calculated at $T = 210$ K and the SNC for fcc Pt in brackets were calculated at $T = 255$ K. For comparison, the results of the magnetic moment direction-constrained calculation for Mn_3Ga in configuration A (denoted A*) and the ferromagnetic calculation for Mn_3Ga with the magnetic moments in the \hat{x} -direction (denoted FM) are given as well. Some previous experimental results are also listed for comparison.

| | | $N(E_F)$ | σ_H^A (S/cm) | $\sigma_H^A(\mu)'$ (S/cm-eV) | α_N^A (A/m-K) | σ_{xy}^z (\hbar/e)(S/cm) | $\sigma_{xy}^z(\mu)'$ (\hbar/e)(S/cm-eV) | α_{xy}^z (\hbar/e)(A/m-K) |
|----------|----|----------|--|---------------------------------|---|--|---|---|
| Mn_3Sn | A | 1.96 | -132, -68 ^a , -90 ^b | -456 | -4.6 (-1.16), -0.39 ^b , -0.28 ^c | 72 | -845 | 7.7 |
| | B | 1.96 | -132, -126 ^a , -80 ^b | -444 | -4.7 (-1.18), -0.32 ^b | 74 | -834 | 7.5 |
| Mn_3Ge | A | 2.37 | -298, 310 ^d , 150 ^e | -9020 | -6.4 | 56 | 691 | 1.02 |
| | B | 2.38 | -298, 380 ^d , 500 ^e | -8289 | -6.4 | 63 | 1000 | 0.63 |
| Mn_3Ga | A | 5.99 | -104 | -3722 | 17.1 | -219 | -5323 | 7.3 |
| | A* | 5.99 | -106 | -3697 | 17.3 | -219 | -5134 | 7.4 |
| | B | 5.99 | -103 | -3953 | 17.0 | -241 | -3561 | 6.6 |
| | FM | 6.82 | 181 | -12836 | -14.0 | -678 | -10601 | 3.2 |
| bcc Fe | | 1.11 | 708, 1200 ^e | -230 | 0.40, 1.8 ^f | - | - | - |
| fcc Pt | | 1.75 | - | - | - | 2139 | 1214 | -1.11 (-0.92), -1.57 ^g |

^aRef. 11 (experiment at 50 K), ^bRef. 22 (experiment at 210 K), ^cRef. 23 (experiment at 200 K), ^dRef. 12 (experiment at 10 K), ^eRef. 13 (experiment at 2 K). ^fRef. 22 (experiment at 300 K). ^gExtracted from the experiment at 255 K [46].

nets would find promising applications in thermoelectric devices, heat nanosensors and also spin caloritronics.

One may wonder whether the nonzero ANC and AHC are caused by the presence of the small net magnetization in these noncollinear antiferromagnetic structures, as in the case of ferromagnets where the ANC and AHC are proportional to the net magnetization. To address this issue, we perform the magnetic moment direction-constrained GGA calculation for the A structure of Mn_3Ga in order to make the total magnetic moment vanished. The results of this calculation are listed in Tables I and II. Table II shows that the resultant ANC and AHC remain nearly unchanged, although the net magnetic moment is reduced by a factor of ~ 20 (Table I). Moreover, we also carry out the GGA calculation for Mn_3Ga in the ferromagnetic state (FM) with magnetization along the \hat{x} -axis. Interestingly, although the total magnetic moment of the FM state is three orders of magnitude larger than that of the A structure (Table I), the ANC gets reduced by 20 %, compared with that of the A structure.

The calculated ANC (α_{yz}^A) and AHC (σ_{yz}^A) of magnetic structure A as a function of the Fermi energy (E_F) as well as the relativistic band structure are plotted in Fig. 3 for Mn_3Sn , in Fig. 4 for Mn_3Ge and in Fig. 5 for Mn_3Ga . Figure 3 shows that for up to 0.33 eV above the E_F , the σ_{yz}^A of Mn_3Sn is negative and rather flat with small ripples. However, if the Fermi energy is lowered to -0.114 eV, one sees a very pronounced negative peak in σ_{yz}^A . The peak σ_{yz}^A value is -979 S/cm. To reach this energy level, the number of valence electrons should be reduced by 0.206 per formula unit (f.u.), indicating substitution of ~ 20 % of Sn by In or Ga. Examination of the calculated band-resolved Berry curvatures suggests

that this peak arises predominantly from the large Ω_{yz} on the top valence band in the vicinity of the gap at M-point [see Fig. 3(a)]. The shape of the σ_{yz}^A versus E_F curve in Mn_3Ge [Fig. 4(b)] is similar to that of Mn_3Sn [Fig. 3(b)], and this is understandable because both alloys are isoelectronic. Mn_3Ga has roughly the same σ_{yz}^A versus E_F curve [Fig. 5(b)] as that of Mn_3Ge and Mn_3Sn except that the Fermi level is now about 0.25 eV lower mainly because Mn_3Ga has one less valence electron.

To understand the features in the α_{yz}^A versus E_F curve, one should note that at low temperatures, Eq. (2) can be simplified as the Mott relation,

$$\alpha_{xy}^A = -\frac{\pi^2}{3} \frac{k_B^2 T}{e} \sigma_{xy}^A(\mu)', \quad (5)$$

which relates the ANC to the energy derivative of the AHC. This Mott relation roughly explains why in Mn_3Sn [Fig. 3(c)] there is a prominent peak in α_{yz}^A at -0.070 eV, where σ_{yz}^A has a steep slope [Fig. 3(b)]. The peak α_{yz}^A value is as large as -19 A/m-K at 300 K. One could reach this point by reducing the valence electrons by 0.13 electron per Mn_3Sn , i.e., by merely substituting 13 % Sn with In or Ga. As mentioned before, σ_{yz}^A is rather flat above the Fermi level [Fig. 3(b)], and this explains why α_{yz}^A becomes nearly zero slightly above the E_F [Fig. 3(c)].

We have also calculated the ANC of all the alloys as a function of temperature (T) and the results are displayed in Fig. 6(a) together with the calculated T -dependent α_{xy}^A of bcc Fe. Figure 6(a) shows that at high temperature (300~400 K) Mn_3Ga has a very large α_{yz}^A , being up to ~ 20 A/m-K which is 50 times larger than that of bcc Fe. The α_{yz}^A of Mn_3Ga decreases steadily with decreasing T and eventually approaches zero at ~ 50 K. The magnitude of the ANC of Mn_3Sn and Mn_3Ge is also large

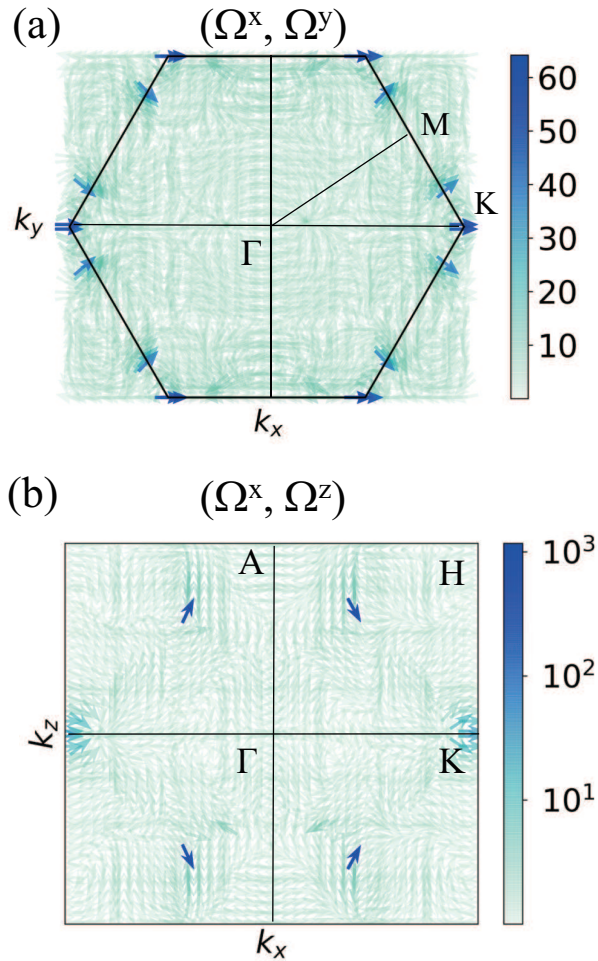


FIG. 2: (Color online) Berry curvature $[\Omega^x(\mathbf{k}), \Omega^y(\mathbf{k}), \Omega^z(\mathbf{k})]$ (in units of \AA^2) of configuration A Mn_3Sn . (a) (Ω^x, Ω^y) on the $k_x k_y$ ($k_z = 0$) plane and (b) (Ω^x, Ω^z) on the $k_x k_z$ ($k_y = 0$) plane.

at high temperatures (e.g., $\sim 10 \text{ A/m-K}$ at $T = 400 \text{ K}$) but the sign of the ANC is negative, being opposite to that of Mn_3Ga . The magnitudes of the ANC of Mn_3Sn and Mn_3Ge decrease monotonically as T decreases and change sign at 175 K and 200 K, respectively. As T further cools, the ANC of Mn_3Ge increases steadily and reaches to 5.2 A/m-K at 50 K, while that of Mn_3Sn stays around 0.6 A/m-K with small fluctuations. Because of their large ANC at room temperature [being at least one order of magnitude larger than that of bcc Fe (see Table II)], all three Mn_3X alloys could serve as a thermoelectric material for spin caloritronics.

To examine the validity of the Mott relation [Eq. (5)], we calculated the energy derivative of the AHC for all the alloys and bcc Fe, as listed in Table II. The ANC at 100 K calculated using Eq. (5) and the energy derivatives of the AHC are shown in Fig. 6(a). Figure 6(a) indicates that the ANC values calculated this way agree in sign with those calculated directly using Eq. (2) for Mn_3Sn , Mn_3Ge and bcc Fe. However, the magnitudes

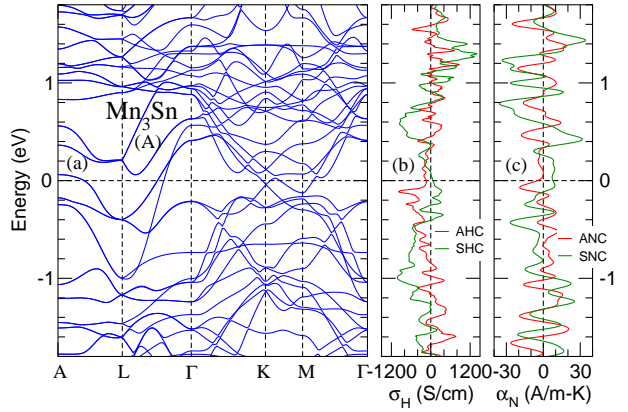


FIG. 3: (Color online) Mn_3Sn . (a) Relativistic band structure in magnetic structure A. (b) Anomalous Hall conductivity (AHC) (σ_{yz}^A) and spin Hall conductivity (SHC) (σ_{xy}^z) as well as (c) anomalous Nernst conductivity (ANC) (α_{yz}^A) and spin Nernst conductivity (SNC) (α_{xy}^z) as a function of energy. The Nernst conductivities were calculated at $T = 300 \text{ K}$. The Fermi level is at the zero energy. Note that in (b) [(c)], the unit for the SHC [SNC] should be $(\hbar/e)\text{S/cm}$ [$(\hbar/e)\text{A/m-K}$].

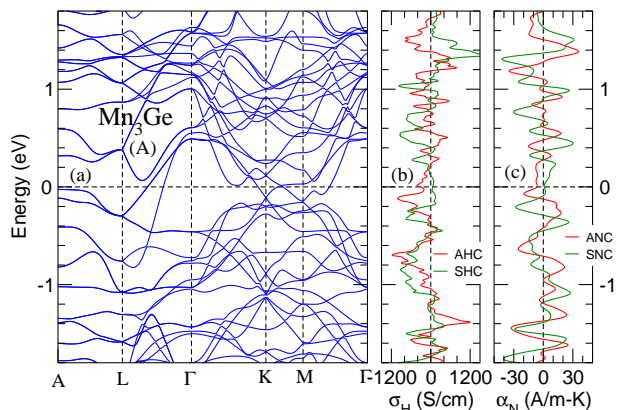


FIG. 4: (Color online) Mn_3Ge . (a) Relativistic band structure in the A magnetic structure. (b) Anomalous Hall conductivity (AHC) (σ_{yz}^A) and spin Hall conductivity (SHC) (σ_{xy}^z) as well as (c) anomalous Nernst conductivity (ANC) (α_{yz}^A) and spin Nernst conductivity (SNC) (α_{xy}^z) as a function of energy. The Nernst conductivities were calculated at $T = 300 \text{ K}$. The Fermi level is at the zero energy. Note that in (b) [(c)], the unit for the SHC [SNC] should be $(\hbar/e)\text{S/cm}$ [$(\hbar/e)\text{A/m-K}$].

differ significantly. At 300 K, the ANC for all Mn_3X alloys estimated using Eq. (5) would differ in sign from those from Eq. (2) (listed in Table II). We note that in the magnetized Pt and Pd, at 100 K the α_{xy}^A calculated using the Mott relation [Eq. (5)] and directly from Eq. (2) agree quantitatively, and even at 300 K they agree with each other quite well.³³

The band structures of magnetic structures A and B of all three alloys are almost identical and thus their band structures for the B configuration are not presented in this paper. Furthermore, the two magnetic configura-

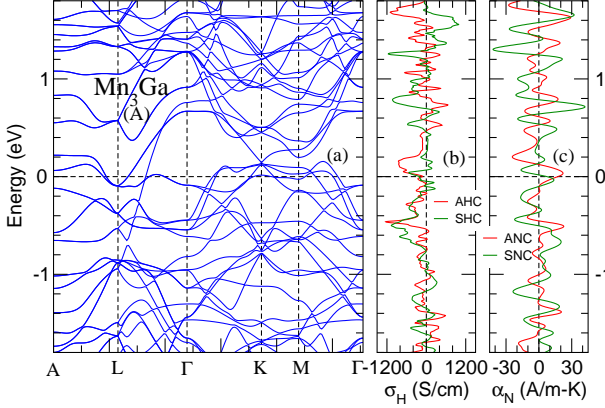


FIG. 5: (Color online) Mn₃Ga. (a) Relativistic band structure in the A magnetic structure. (b) Anomalous Hall conductivity (AHC) (σ_{zz}^A) and spin Hall conductivity (SHC) (σ_{xy}^z) as well as (c) anomalous Nernst conductivity (ANC) (α_{zx}^A) and spin Nernst conductivity (SNC) (α_{xy}^z) as a function of energy. The Nernst conductivities were calculated at $T = 300$ K. The Fermi level is at the zero energy. Note that in (b) [(c)], the unit for the SHC [SNC] should be $(\hbar/e)\text{S}/\text{cm}$ [$(\hbar/e)\text{A}/\text{m}\cdot\text{K}$].

tions for each alloy have similar AHC and ANC as a function of energy and hence the AHC and ANC as a function of energy of the B configuration are not displayed here either. The present band structures of Mn₃Sn (Fig. 3) and Mn₃Ge (Fig. 4) are in good agreement with the previous GGA results^{14,47}. The present (Fig. 5) and previous¹⁴ GGA band structures for Mn₃Ga also agree quite well along all the high symmetry lines except the KM line where the two band structures differ quite significantly.

As mentioned before, the AHE in Mn₃Sn and Mn₃Ge in noncollinear antiferromagnetic states have been experimentally investigated by several groups.^{11–13,22} The calculated AHC (132 S/cm) for Mn₃Sn in configuration B agrees well with the measured value (126 S/cm at 50 K) reported in Ref. [11], although the theoretical AHC (132 S/cm) in configuration A is nearly twice as large as the measured value (68 S/sm) (see Table II). The calculated AHC for Mn₃Ge in both configuration A and B is also in good agreement with the experimental value at 10 K reported in Ref. [12], although for configuration B it is about 30 % smaller than the measured one (500 S/cm at 2 K) presented in Ref. [13] and for configuration A it is twice as large as the measured one¹³. All these suggest that the anomalous Hall effect in these alloys is dominated by the intrinsic mechanism due to the nonzero Berry curvatures in the momentum space.^{5,32} This is also the conclusion drawn in Ref. [22] based on the experimental examination on the validity of the Wiedemann-Franz law. The AHC of Mn₃Sn (Mn₃Ge) presented in Table II is in excellent agreement with the GGA result of 133 (330) S/cm of Mn₃Sn (Mn₃Ge) reported in Refs. [14,47].

However, unlike the AHE case, so far merely two papers very recently reported on the experiments on the

ANE in Mn₃Sn.^{22,23} It was found that the ANE signals are significant and easily detectable.^{22,23} Furthermore, the thermal and Nernst conductivities was found to correlate according to the Wiedemann-Franz law, indicating the intrinsic origin of the ANE. Overall, this is consistent with our finding of large intrinsic ANE in these alloys. Also the measured and calculated ANC at ~ 210 K agree in sign with respect to that of AHC, although the measured ANC (0.39 and 0.28 A/m-K) for configuration A is a few times smaller than the calculated ANC (1.16 A/m-K) (Table II). Nevertheless, experimentally, the ANC and AHC were found to decrease steadily as the T is increased from 200 K to 400 K,^{22,23} in contrast to the monotonical increase of the calculated ANC with T [Fig. 6(a)]. This significant discrepancy could arise from several reasons. First of all, the temperature range of 200~400 K is close to the antiferromagnetic transition (T_N) and consequently the magnetism gets weaker as the T_N is approached. In the theoretical calculation, however, the $T = 0$ magnetism is assumed and the T -dependence enters only through the Fermi function [see Eq. (2)]. Secondly, although the ANC is calculated directly from the band structure [see Eq. (2)], experimentally, the ANC cannot be measured directly and thus is estimated using measurable longitudinal (ρ_{ii}) and Hall (ρ_{ij}) resistivities as well as Seebeck (S_{ii}) and Seebeck-Nernst (S_{ij}) coefficients via^{22,23}

$$\alpha_{yz}^A = -\frac{\rho_{zz}S_{yz} - \rho_{yz}S_{zz}}{\rho_{yy}\rho_{zz} - \rho_{yz}\rho_{zy}} \approx \frac{\rho_{zz}S_{yz} - \rho_{zz}S_{yz}}{\rho_{yy}\rho_{zz}}. \quad (6)$$

Clearly, to obtain accurate estimated ANC, all these quantities must be accurately measured on the same sample, but this often is not the case. Given all these complications, we believe that the level of agreement between the experiment and calculation is quite good. Table II shows that the experimental ANC of iron at 300 K also reported in [22] is ~ 1.8 A/m-K, being four times larger than the present theoretical ANC (0.4 A/m-K). Furthermore, a previous GGA calculation of the intrinsic ANC⁴⁸ of iron gave a value of 0.16 A/m-K, being more than two times smaller than the present GGA result. Further experiments on the ANE and AHE on these alloys are clearly needed.

C. Spin Nernst effect

The SNC (α_{xy}^s ; $s, i, j = x, y, z$) and SHC (σ_{xy}^s) are third-order tensors. A recent symmetry analysis¹⁴ showed that only elements $\sigma_{yz}^x(\sigma_{zy}^x)$, $\sigma_{xz}^y(\sigma_{yz}^y)$ and $\sigma_{xy}^z(\sigma_{yx}^z)$ can be nonzero. Furthermore, the *ab initio* calculations of the SHC of Mn₃X ($X = \text{Sn, Ge, Ga}$)¹⁴ indicated that only σ_{xy}^z and σ_{yx}^z are significantly nonzero. Therefore, in this paper we consider only α_{xy}^z and α_{yx}^z . The calculated α_{xy}^z and σ_{xy}^z of all Mn₃X alloys are listed in Table II. The α_{xy}^z and σ_{xy}^z of platinum metal³³ are also listed there for comparison. Table II shows that the SHC of the Mn₃X alloys is rather small, compared to

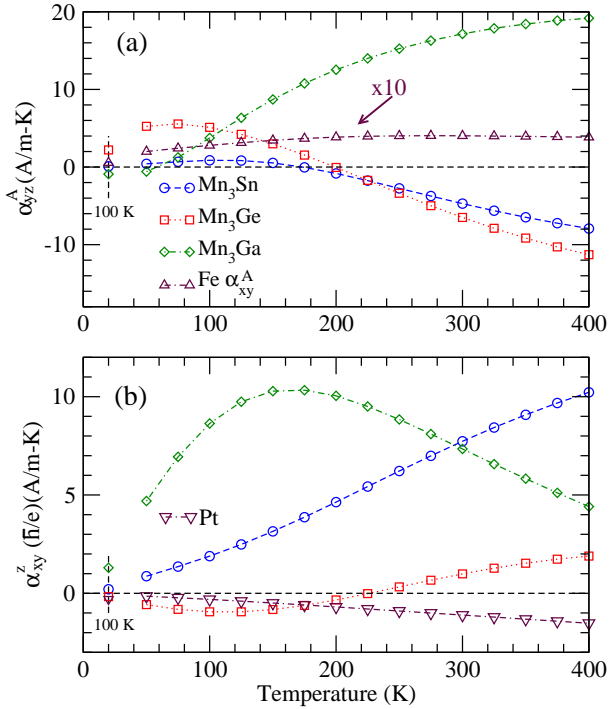


FIG. 6: (color online) (a) Anomalous Nernst conductivity (ANC) (α_y^A) and (b) spin Nernst conductivity (SNC) (α_{xy}^S) as a function of temperature. The values displayed on the vertical dashed line (a) and (b) are the ANC and SNC at 100 K calculated using the Mott relations [Eq. (5) and Eq. (6)] and the energy derivatives of AHC and SHC listed in Table II, respectively.

that of platinum, which has the largest intrinsic SHC among transition metals.^{7,26} Remarkably, the SNC of Mn₃Sn and Mn₃Ga is very large, being about five times larger than that of Pt (Table II). Mn₃Ge also has a larger SNC than platinum. This shows that noncollinear anti-ferromagnets Mn₃X ($X = \text{Sn, Ge, Ga}$) would be very useful materials for spin thermoelectric devices and spin caloritronics, just like Pt metal for spintronics.

The calculated SNC (α_{xy}^S) and SHC (σ_{xy}^z) as a function of the Fermi energy (E_F) of Mn₃Sn, Mn₃Ge and Mn₃Ga are displayed in Fig. 3, Fig. 4 and Fig. 5, respectively. Figures 3(b) and 4(b) show that in both Mn₃Sn and Mn₃Ge the σ_{xy}^z in the vicinity of the E_F is rather small, thus resulting in a small value at the E_F (Table II). Nevertheless, the σ_{xy}^z in Mn₃Ge has a broad prominent peak near -0.30 eV, and the peak value is as large as -750 (\hbar/e)S/cm [Fig. 4(b)]. This peak can be reached by a reduction of the valence electrons of ~ 1.0 e/f.u. For Mn₃Ga which has one less valence electron, the E_F is lowered to just below this peak [Fig. 5(b)], thus resulting in a much larger σ_{xy}^z value (Table II).

To understand the features in the α_{yz}^z versus E_F curve, one should note again that Eq. (4) would be reduced to

the simple Mott relation at low temperatures,

$$\alpha_{xy}^z = -\frac{\pi^2}{3} \frac{k_B^2 T}{e} \sigma_{xy}^z(\mu)', \quad (7)$$

which relates the SNC to the energy derivative of the SHC. This Mott relation roughly explains why in Mn₃Sn [Fig. 3(c)] the α_{yz}^z has a broad plateau from -0.09 eV to 0.23 eV around the E_F , where σ_{yz}^z has more or less a constant negative slope [Fig. 3(b)]. The plateau α_{yz}^z value is about 9 (\hbar/e)A/m-K at 300 K. In Mn₃Ge, the α_{yz}^z is rather small in the vicinity of the E_F because σ_{yz}^z is rather flat (and small) (Fig. 4). Nevertheless, the α_{yz}^z has a prominent negative peak at -0.21 eV [Fig. 4(c)] where σ_{yz}^z has a steep slope [Fig. 4(b)]. Within the rigid band model, the α_{yz}^z peak could be reached by reducing the number of valence electrons by ~ 0.51 e/f.u. In Mn₃Ga, the E_F sits on the upper side of the pronounced peak at -0.035 eV and thus α_{yz}^z is large, being as large as 14 (\hbar/e)A/m-K at 300 K. Again, this is because the σ_{yz}^z has a steep slope at -0.035 eV [Fig. 5(b)].

Very recently, the SNE in platinum was studied experimentally and a large spin Nernst angle (θ_{SN}) was observed.⁴⁶ The spin Nernst angle is comparable in size but opposite in sign to the spin Hall angle (θ_{SH}) with $\theta_{SH}/\theta_{SN} = -0.5$ at 255 K.⁴⁶ It can be shown that $\alpha_{xy}^z = -\sigma_{xy}^z S_{yy}/(\theta_{SH}/\theta_{SN})$. Using the theoretical $\sigma_{xy}^z = 2139$ (\hbar/e)(S/cm) (Table II) and measured Seebeck coefficient $S_{yy} = -3.67 \mu\text{V/K}$ at 255 K,⁴⁹ we would obtain an estimated experimental $\alpha_{xy}^z = -1.57$ (\hbar/e)(S/cm), agreeing quite well with the calculated value of -0.92 (\hbar/e)A/m-K (Table II).

In Fig. 6(b), the calculated T -dependence of the SNC for all three alloys as well as Pt metal are displayed. Fig. 6(b) shows that the magnitude of the SNC of Mn₃Sn is very large at high temperatures (e.g., ~ 10 (\hbar/e)A/m-K at $T = 400$ K). Nevertheless, the SNC decreases monotonically as the T decreases down to 50 K. Interestingly, the SNC of Pt has a very similar T -dependence, albeit with a much smaller magnitude and an opposite sign. In contrast, Mn₃Ga has a smaller SNC at high temperatures (e.g., ~ 4.4 (\hbar/e)A/m-K at $T = 400$ K). However, the SNC of Mn₃Ga increases steadily as the T is lowered, and it reaches its maximum of ~ 10 (\hbar/e)A/m-K at $T = 175$ K. It then decreases monotonically as the T further decreases. Mn₃Ge has a small SNC at high temperatures (e.g., ~ 1.9 (\hbar/e)A/m-K at $T = 400$ K). The SNC of Mn₃Ge decreases gradually as the T decreases and changes sign at $T = 225$ K. After passing 225 K, it further decreases as the T is lowered to 125 K, and it then increases slightly as the T decreases to 50 K.

We calculated the energy derivative of the SHC for all the alloys and fcc Pt, as listed in Table II, in order to examine the validity of the Mott relation [Eq. (7)]. The SNC at 100 K calculated using Eq. (7) and the energy derivatives of the SHC are shown in Fig. 6(b). Figure 6(b) indicates that all the SNC values calculated this way agree in sign with those calculated directly using Eq. (4). For fcc Pt, the SNC values [-0.30 and -0.31 (\hbar/e)S/cm]

agree rather well. This level of agreement [-0.89 and -1.11 (\hbar/e)S/cm] is maintained even at 300 K. For Mn_3Ga (Mn_3Ge), the SNC value from Eq. (7) is 2.5 (five) times smaller than that from Eq. (4). For Mn_3Sn , the SNC values from Eq. (7) and Eq. (4) differ by one order of magnitude [Fig. 6(b)].

IV. CONCLUSIONS

We have studied theoretically the ANE, a phenomenon having the same origin as the AHE, and also the SNE as well as the AHE and SHE in noncollinear antiferromagnetic Mn_3X ($X = Sn, Ge, Ga$) based on *ab initio* relativistic band structure calculations. As references, we also calculate the ANC and AHC of ferromagnetic iron as well as the SNC of platinum metal. Fascinatingly, the calculated ANC at room temperature (300 K) for all three alloys is huge, being 10~40 times larger than that of iron. Further, the calculated SNC for Mn_3Sn and Mn_3Ga is also larger, being about five times larger than that of platinum. This suggests that these anti-

ferromagnets would be useful materials for thermoelectronic devices and spin caloritronic devices. The calculated ANC of Mn_3Sn and iron are in reasonably good agreement with the very recent experiments²². The calculated SNC of platinum also agree well with the very recent experiments⁴⁶ in both sign and magnitude. The calculated thermoelectric and thermomagnetic properties are analyzed in terms of the band structures as well as the energy-dependent AHC, ANC, SNC and SHC via the Mott relations. We hope that our interesting theoretical results would stimulate further experimental works on these noncollinear antiferromagnets.

Acknowledgments

The authors acknowledge support from the Ministry of Science and Technology and the Academia Sinica of The R.O.C. as well as the NCTS and the Kenda Foundation in Taiwan. G.Y.G thanks Qian Niu for stimulating discussions.

* Electronic address: gyguo@phys.ntu.edu.tw

¹ G. A. Prinz, *Science* **282**, 1660 (1998); S. A. Wolf, D. D. Awschalom, R. Chtchelkanova, and D. M. Treger, *ibid.*, **294**, 1488 (2001)

² I. Zutic, J. Fabianm and S. D. Sarma, *Rev. Mod. Phys.* **76**, 323 (2004).

³ E. H. Hall, *Phil. Mag.* **B** 12, 157 (1881).

⁴ M. I. Dyakonov and V. I. Perel, *Sov. Phys. JETP* **33**, 1053 (1971).

⁵ N. Nagaosa, J. Sinova, S. Onoda, A. H. MacDonald, and N. P. Ong, *Rev. Mod. Phys.* **82**, 1539 (2010)

⁶ J. Sinova, S. O. Valenzuela, J. Wunderlich, C. H. Back and T. Jungwirth, *Rev. Mod. Phys.* **87**, 1213 (2015)

⁷ A. Hoffman, *IEEE Trans. Mag.* **49**, 5172 (2013).

⁸ S. Murakami, N. Nagaosa, and S.-C. Zhang, *Science* **301**, 1348 (2003)

⁹ L. Liu, C.-F. Pai, Y. Li, H.-W. Tseng, D. C. Ralph, and R. A. Buhrman, *Science* **336**, 555 (2012)

¹⁰ H. Chen, Q. Niu, and A. H. MacDonald, *Phys. Rev. Lett.* **112**, 017205 (2014).

¹¹ S. Nakatsuji, N. Kiyohara and T. Higo, *Nature* **527**, 212 (2015).

¹² N. Kiyohara, T. Tomita and S. Nakatsuji, *Phys. Rev. Applied* **5**, 064009 (2016).

¹³ A. K. Nayak, J. E. Fischer, Y. Sun, B. Yan, J. Karel, A. C. Komarek, C. Shekhar, N. Kumar, W. Schnelle, J. Kübler, C. Felser and S. S. P. Parkin, *Sci. Adv.* **2**, e1501870 (2016).

¹⁴ Y. Zhang, Y. Sun, H. Yang, J. Zelezny, S. S. P. Parkin, C. Felser and B. Yan, *Phys. Rev. B* **95**, 075128 (2017).

¹⁵ W. Zhang, W. Han, S.-H. Yang, Y. Sun, Y. Zhang, B. Yan and S. S. P. Parkin, *Sci. Adv.* **2**, e1600759 (2016).

¹⁶ T. Jungwirth, X. Marti, P. Wadley and J. Wunderlich, *Nature Mano.* **11**, 231 (2016).

¹⁷ W. Nernst, *Ann. Phys.* **267**, 760 (1887).

¹⁸ W.-L. Lee, S. Watauchi, V. L. Miller, R. J. Cava, and N. P. Ong, *Phys. Rev. Lett.* **93**, 226601 (2004).

¹⁹ D. Xiao, Y. Yao, Z. Fang and Q. Niu, *Phys. Rev. Lett.* **97**, 026603 (2006).

²⁰ S.-g. Cheng, Y. Xing, Q.-f. Sun and X. C. Xie, *Phys. Rev. B* **78**, 045302 (2008).

²¹ G. E. W. Bauer, E. Saitoh and B. J. van Wees, *Nature Mater.* **11**, 391 (2012)

²² X. Li, L. Xu, L. Ding, J. Wang, M. Shen, X. Lu, Z. Zhu and K. Behnia, *Phys. Rev. Lett.* **119**, 056601 (2017).

²³ M. Ikhlas, T. Tomita, T. Koretsune, M.-T. Suzuki, D. Nishio-Hamane, R. Arita, Y. Otani and S. Nakatsuji, *Nat. Phys.* **13**, 1085 (2017).

²⁴ J. P. Perdew, K. Burke, M. Ernzerhof, *Phys. Rev. Lett.* **77**, 3865 (1996).

²⁵ Y. Yao, K. Kleinman, A. H. MacDonald, J. Sinova, T. Jungwirth, D.-S. Wang, E.-G. Wang and Q. Niu, *Phys. Rev. Lett.* **92**, 037204 (2004).

²⁶ G. Y. Guo, S. Murakami, T.-W. Chen, and N. Nagaosa, *Phys. Rev. Lett.* **100**, 096401 (2008).

²⁷ E. Kren and G. Kadar, *Solid State Commun.* **8**, 1653 (1970).

²⁸ P. E. Blöchl, *Phys. Rev. B* **50**, 17953 (1994).

²⁹ G. Kresse, J. Hafner, *Phys. Rev. B* **47**, 558 (1993).

³⁰ G. Kresse, J. Furthmüller, *Phys. Rev. B* **54**, 11169 (1996).

³¹ O. Jepson and O. K. Anderson, *Solid State Commun.* **9**, 1763 (1971)

³² D. Xiao, M.-C. Chang, and Q. Niu, *Rev. Mod. Phys.* **82**, 1959 (2010)

³³ G. Y. Guo, Q. Niu, and N. Nagaosa, *Phys. Rev. B* **89**, 214406 (2014).

³⁴ B. Adolph, J. Furthmüller and F. Bechsted, *Phys. Rev. B* **63**, 125108 (2001).

³⁵ G. Y. Guo, Y. Yao, and Q. Niu, *Phys. Rev. Lett.* **94**, 226601 (2005).

³⁶ H.-R. Fuh and G. Y. Guo, *Phys. Rev. B* **84**, 144427 (2011).

³⁷ J.-C. Tung, H.-R. Fuh and G. Y. Guo, Phys. Rev. B **86**, 024435 (2012).

³⁸ J. Sticht, K.-H. Höck and J. Kübler, J. Phys.: Condens. Matter **1**, 8155 (1989).

³⁹ L. M. Sandratskii and J. Kübler, Phys. Rev. Lett. **76**, 4963 (1996).

⁴⁰ J. Kübler and C. Felser, Europhys. Lett. **108**, 67001 (2014).

⁴¹ G. J. Zimmer and E. Kren, AIP Conf. Proc. **5**, 513 (1971).

⁴² G. Kadar and E. Kren, Int. J. Magn. **1**, 143 (1971).

⁴³ S. Tomiyoshi, Y. Yamaguchi, T. Nagamiya, J. Magn. Magn. Mater. **31-34**, 629 (1983).

⁴⁴ T. Nagamiya, S. Tomiyoshi, Y. Yamaguchi, Solid State Commun. **42**, 385 (1982).

⁴⁵ W. Feng, G. Y. Guo, J. Zhou, Y. Yao and Q. Niu, Phys. Rev. B **92**, 144426 (2015).

⁴⁶ S. Meyer, Y.-T. Chen, S. Wimmer, M. Althammer, T. Wimmer, R. Schlitz, S. Geprägs, H. Huebl, D. Ködderitzsch, H. Ebert, G. E. W. Bauer, R. Gross and S. T. B. Goennenwein, Nat. Mater. **16**, 977 (2017).

⁴⁷ H. Yang, Y. Sun, Y. Zhang, W.-J. Shi, S. S. P. Parkin and B. Yan, New J. Phys. **19**, 015008 (2017).

⁴⁸ J. Weischenberg, F. Freimuth, S. Blügel, and Y. Mokrousov, Phys. Rev. B **87**, 060406 (2013).

⁴⁹ J. P. Moore and R. S. Graves, J. Appl. Phys. **44**, 1174 (1973).